

See discussions, stats, and author profiles for this publication at: <https://www.researchgate.net/publication/263955895>

ZnO:Er,Yb,Gd Particles Designed for Magnetic-Fluorescent Imaging and Near-Infrared Light Triggered Photodynamic Therapy

ARTICLE in THE JOURNAL OF PHYSICAL CHEMISTRY C · NOVEMBER 2013

Impact Factor: 4.77 · DOI: 10.1021/jp4071696

CITATIONS

9

READS

65

3 AUTHORS, INCLUDING:



[Wei Wang](#)

Qingdao University of Science and Technology

16 PUBLICATIONS 177 CITATIONS

SEE PROFILE



[Kezheng Chen](#)

Qingdao University of Science and Technology

104 PUBLICATIONS 1,284 CITATIONS

SEE PROFILE

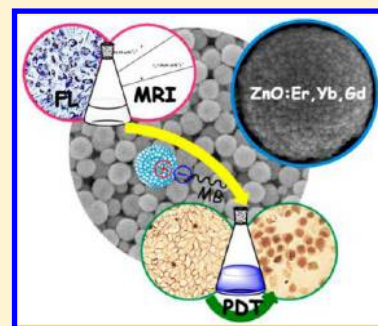
ZnO:Er,Yb,Gd Particles Designed for Magnetic-Fluorescent Imaging and Near-Infrared Light Triggered Photodynamic Therapy

Xiaojun Wei, Wei Wang, and Kezheng Chen*

Lab of Functional and Biomedical Nanomaterials, College of Materials Science and Engineering, Qingdao University of Science and Technology, Qingdao 266042, China

Supporting Information

ABSTRACT: In this paper, fluorescent and magnetic bifunctional ZnO:Er,Yb,Gd particles were synthesized via a simple homogeneous precipitation method. The morphology, size, fluorescent properties, and magnetic properties of the particles can be readily modified by doping with Er³⁺, Yb³⁺, and Gd³⁺. The results revealed that the ZnO:Er,Yb,Gd particles have both down-conversion and up-conversion fluorescence after calcination at high temperatures (>700 °C). The products successfully labeled the human hepatocellular carcinoma (HepG2) cells and presented low toxicity even at a high concentration of 2 mg/mL. Being upconverting nanoparticles (UCNPs), the prepared ZnO:Er,Yb,Gd particles exposed to 980 nm near-infrared (NIR) laser light emitted up-conversion fluorescence which could be absorbed by a photodynamic therapy (PDT) drug, methylene blue (MB), and then killed the HepG2 cells via PDT mechanism. In vitro therapeutic investigation evidenced the prominent PDT effects of MB-loaded ZnO:Er,Yb,Gd UCNPs upon NIR light irradiation. In magnetic resonance imaging (MRI) studies, ZnO:Er,Yb,Gd particles revealed a tunable longitudinal relaxivity rate (r_1) from 23.03 mM⁻¹ s⁻¹ to 36.84 mM⁻¹ s⁻¹, which is much larger than the conventional Gd-DTPA and currently reported Gd-base nanoparticles, suggesting it would be a good candidate as an MRI agent. It is expected that these particles have applications in magnetic-fluorescent bimodal imaging and NIR light triggered photodynamic therapy.



INTRODUCTION

Nanotechnology holds tremendous potential for early detection, accurate diagnosis, and personalized treatment of cancer.^{1–3} In this regard, a number of molecular imaging techniques, such as fluorescence imaging (FI), magnetic resonance imaging (MRI), ultrasound imaging (USI), positron emission tomography (PET), and others have been reported for imaging of in vitro and in vivo biological specimens.^{4,5} Different imaging techniques are, in general, complementary rather than competitive and the choice of imaging modality depends primarily on the specific question that is to be addressed.⁶ Therefore, various multimodal imaging probes combining different imaging modalities have been developed for more accurate imaging and diagnosis. For example, nanoparticles combining FI modality and MRI modality can offer the advantages of fluorescence imaging, i.e., high sensitivity, along with the high spatial resolution anatomic imaging capability of MRI.^{7–10} At present, much effort has been spent in the investigation of magnetic-fluorescent nanoparticles which can serve as magnetic resonance contrast agents for MRI and optical probes for intravital fluorescence microscopy.^{11–15}

Recently, lanthanide ion-doped nanoparticles have received much attention due to their excellent luminescence properties, including large Stokes shifts, narrow line-width emission bands, high quantum yields, long lifetimes, and superior photostability.¹⁶ Nanoparticles that contain lanthanide ions are advantageous for biological applications over the undoped ones, because the sharp emission signal corresponding to each

lanthanide ion has a unique spectroscopic signature for spectral and unambiguous identification.^{17–19} Particularly the lanthanide ion-doped upconversion nanoparticles (UCNPs), which are able to convert two or more low-energy pump photons from the near-infrared (NIR) spectral region (700–1000 nm) to a higher-energy output photon with a shorter wavelength, have found potential applications in many different fields, including biomedicine and bioimaging.^{20–23} Compared with traditional fluorescence imaging using organic dyes or quantum dots, the NIR light excited upconversion luminescence imaging relying on UCNPs exhibits improved tissue penetration depth, uses particles with higher photochemical stability, and is free of autofluorescence. Thus it affords remarkably improved in vivo sensitivity.^{24,25} UCNPs could be further engineered to acquire additional functionalities. By introducing Gd³⁺, UCNPs could be used as MRI contrast agents as the Gd³⁺ ions in the host materials can accelerate longitudinal (T_1) relaxation of water protons and exert bright contrast in regions where the nanoprobe localizes.^{26,27} In addition, chemotherapy drugs or photosensitizers may be loaded on UCNPs for dual imaging and therapy applications.^{28,29}

With all these fascinating properties, UCNPs hold great potential in biological applications, especially as a nano-transducer for solving the problems that traditional photo-

Received: July 19, 2013

Revised: October 11, 2013

Published: October 18, 2013



dynamic therapy (PDT) has faced, and for inspiring the fabrication of UCNPs/photosensitizer (PS)-based PDT drugs. As we know, PDT is a treatment modality based on the photochemical reactions mediated by the interaction of photosensitizers with specific light and oxygen. Although PDT is a minimally invasive therapeutic modality approved by many countries for numerous clinical cancer treatments, some challenges still persist, including limited penetration depth of the excitation light, poor water solubility of photosensitizers, and so on.^{30,31} Therefore, many efforts have focused on the NIR light triggered PDT with excitation wavelength shifted to the NIR region for deeper tissue treatment. NIR light triggered PDT could effectively reduce the photosensitivity to ambient light and improve the safety of PDT treatment.^{32–35} Unfortunately most of the available PS only absorb visible light rather than NIR light. With the help of UCNPs, NIR light can be converted to visible light that can activate the PDT effect of PS. In other words, UCNPs serve as light nanotransducers in the NIR light triggered PDT. To further enhance the efficiency of PDT treatment, PS drugs may be combined with the UCNPs.

In the past few years, UCNPs/PS have been widely explored as novel drugs^{36–38} and there are many reports on the application of UCNPs/PS nanomaterials for PDT. The examples include UCNPs/M540-based PDT drugs,³⁹ NaYF₄ (Y:Yb:Er = 78%:20%:2%)-PEG-Ce6 nanocrystals,⁴⁰ ZnPc-FA-PEI/NaYF₄:Yb³⁺,Er³⁺ nanoparticles,^{41,44} UCP-TPP-PEG particles,⁴² NaYF₄:Yb,Er/NaGdF₄-Ce6 core-shell UCNPs,⁴³ NaYF₄:Er,Yb@SiO₂-ZnPc nanoparticles^{45,46} and so on. While the area of UCNPs/PS nanocomposites based on the NaYF₄ is still very much in its developing stage, some remaining problems of NaYF₄ such as poor water solubility, low biocompatibilities, and the poor mechanical properties have limited the development of UCNPs/PS nanoparticles to some extent. Some studies have shown that the coating of SiO₂ can improve the biological application performance of NaYF₄; unfortunately, not only is the “core-shell” method rather tedious in the sense that it involves synthesizing the functional nanocrystals, and then putting them into one entity,⁴⁷ but the efficiency of PDT for these particles is also low because the nonporous or mesoporous silica shell blocks egress from the particles of the reactive ¹O₂ species generated.⁴⁵

For applications, zinc oxide (ZnO) is well-recognized as a biocompatible multifunctional material because there are several important features of ZnO for the applications in bioimaging and biomedicine: (1) superior chemical stability and photostability in vitro or in vivo; (2) resistance to photobleaching; (3) high absorbency and low-toxicity; (4) adequate dispersibility in the biological environment, and so on. ZnO is also a wide band gap semiconductor (3.37 eV) with high exciton binding energy (60 meV), which leads to efficient excitonic blue and near-UV emission. These properties make ZnO nanomaterials excellent candidates as biocompatible nanoplateforms for bioimaging applications such as DNA delivery, MRI, and sensing.^{48–56} Liu and colleagues²⁶ reported Gd-doped ZnO quantum dots which showed contrast enhancement in MRI and exhibited significantly enhanced down-conversion yellow emission due to the Gd doping. Moreover the ICP analysis after leaching experiment showed no Gd³⁺ ions in the supernatant after separation, revealing the weak toxicity of Gd-doped ZnO nanoplates. So far, there are limited examples of ZnO-based UCNPs and UCNPs/PS drugs for applications of bioimaging and PDT to our best knowledge.

Zhang and co-workers reported the ZnO:Er³⁺ nanocrystals,⁶⁰ and investigated the effect of annealing on the upconversion luminescence of products; unfortunately, there was no further research on biological applications of the UCNPs.

Herein, we report the synthesis of a series of RE-doped (RE = Er³⁺, Yb³⁺, Gd³⁺) ZnO particles with well-controlled phase, shape, and size by a facile homogeneous precipitation method. The as-synthesized ZnO:Er,Yb,Gd particles have both high efficient up-conversion luminescence and excellent magnetic behavior. In addition, by using a well-selected PDT drug of water-soluble methylene blue (MB), we have succeeded in developing a kind of UCNPs/MB-based PDT drug, ZnO:Er,Yb,Gd-MB, which can kill the HepG2 cells effectively triggered by NIR light. The nanoparticles presented herein may have great potential applications in multimodality biomedical imaging and PDT.

■ EXPERIMENTAL SECTION

Materials. All rare earth oxides used were of 99.99% purity and purchased from Sinopharm Chemical Reagent Co., Ltd. (Beijing, China). Rare earth nitrate RE(NO₃)₃ (RE = Er, Yb, and Gd) solutions were prepared by dissolving the corresponding rare earth oxides in nitric acid at a high temperature. All reagents used for cell experiments were obtained from Sigma Aldrich (USA). The water used in this study was deionized by a milli-Q Plus system, whose electrical resistance is 18.2 MΩ. All other chemicals were analytical grade and used without further purification.

Synthesis of ZnO:Er,Yb,Gd Particles. Zn_{0.85}Er_{0.02}Yb_{0.1}Gd_{0.03} particles were synthesized by a homogeneous precipitation. In a typical process, 1.098 g of Zn(CH₃COO)₂·2H₂O was dissolved in 50 mL of diethylene glycol (DEG). Aqueous solutions of Er(NO₃)₃ (5 mL, 0.02 mol/L), Yb(NO₃)₃ (5 mL, 0.1 mol/L), and Gd(NO₃)₃ (7.5 mL, 0.02 mol/L) were added to the solution of Zn-(CH₃COO)₂·2H₂O with constant stirring for 20 min, and then the mixture was heated to 160 °C in a four-necked, round-bottomed flask under vigorous stirring. The reaction mixture was stirred for 1 h at this temperature after which the heat source was removed and the reaction vessel was cooled to room temperature. The samples were centrifuged at 8000 rpm and then washed with ethanol and deionized water several times. The obtained precipitates were dried at 70 °C for 12 h. The prepared ZnO:Er,Yb,Gd particles were further sintered at high temperatures (>700 °C) for the enhancement of fluorescence properties, which not only have both down-conversion and up-conversion fluorescence but also have spherical morphology with calcination temperature of 800 °C, for 2 h.

Characterization of the Samples. X-ray diffraction (XRD) studies were conducted on a Rigaku D/max-2500 X-ray powder diffractometer, using Cu Kα radiation (λ = 1.5406 Å). X-ray energy dispersive spectroscopy (EDS), attached to the JEOL JSM-6700F electron microscope, was used to determine the elements of the products. Microstructure and elements distribution of the sample were analyzed by using a FEI Tecnai G2 F20 transmission electron microscope equipped with an energy dispersive X-ray spectroscopic analyzer operated at a voltage of 200 KV. The morphological investigations were carried out with field-emission scanning electron microscopy (FESEM, JEOL JSM-6700F). Dynamic light scattering (DLS, Zetasizer Nano, Malvern Instrument) was used to determine the hydrodynamic size and Z-average diameter of the products. Fluorescent properties were performed at room temperature by

a fluorescence spectrophotometer (F4600, Hitachi) with a 980 nm diode laser as the excitation source with a fiber-optic accessory. The Brunauer–Emmett–Teller (BET) method was utilized to calculate the specific surface area, using adsorption data in a relative pressure range from 0 to 1. The magnetic relaxation properties of the product were examined with its aqueous suspension by using a 1.5 T MRI system (Bruker Minispec mq60 NMR analyzer) at 37 °C. Inductively coupled plasma-optic emission spectrometry (ICP-OES, Perkin-Elmer Optima 2000) was used to analyze the element contents of the samples dispersed in ultrapure water. Biocompatibility evaluated by methyl thiazolyl tetrazolium (MTT) viability assay was performed on a Bio-Rad model 680 microplate reader. A UV–vis–NIR spectrophotometer (Cary500, Varian) was utilized to monitor the MB on the UCNPs.

Rare Earth Ions Leakage Test. A dialysis bag with 3000 Da molecular weight cutoff was used. Samples in the PBS were sealed in the dialysis tube and sunk into a 100 mL wide-mouth bottle. Then the bottle was shaken continuously in the water bath with a constant temperature of 37 °C. ICP of rare earth ions from the wide-mouth bottle were monitored as a function of time.

Biocompatibility Assessment of Particles. MTT viability assay, a colorimetric measure of mitochondrial activity, is used to assess the biocompatibility of the nanospheres. HepG2 cells were cultured in a 96-well plate (Costar, approximately 5×10^3 cells per well) with 1640 medium containing 10% fetal bovine serum (FBS) and different concentrations of the ZnO:Er,Yb,Gd particles for different times. Then, 20 μ L of MTT solution (5 mg/mL MTT in phosphate buffer solution (PBS), pH 7.4) was added to each well and the mixtures incubated for 4 h at 37 °C. After removing the medium, intracellular formazan crystals were extracted into 150 μ L of dimethyl sulfoxide (DMSO) and quantified by measuring the absorbance of the cell lysate at 490 nm. Cell viability was expressed as a percentage of the control.

Fluorescent Labeling of HepG2 Cells. The water-soluble ZnO:Er,Yb,Gd nanoparticles were first sterilized with a disinfection boiler and dispersed in culture medium. HepG2 cells were incubated in the incubator (37 °C, 5% CO₂) for different times with ZnO:Er,Yb,Gd nanoparticles with a concentration of 0.2 mg/mL. Then the cells were washed several times with PBS. An inverted microscope (Eclipse TE2000S, Nikon) was used to collect images of cells.

Preparation of PS-Loaded ZnO:Er,Yb,Gd UCNPs. MB was selected as the photosensitizer. MB loading onto the ZnO:Er,Yb,Gd UCNPs was carried out by mixing MB (10 mmol) with UCNPs (0.5 mg/mL) in PBS and stirring at room temperature for 12 h. MB-loaded samples were separated from the free-standing MB molecules through centrifugation at 8000 rpm for 5 min and carefully washed three times by PBS. The formed ZnO:Er,Yb,Gd-MB particles were resuspended in PBS and stored at 4 °C.

The loading capacity of MB on ZnO:Er,Yb,Gd UCNPs was characterized as follows. The supernatants collected from the loading procedure were measured for their UV–visible absorption spectrum, which was compared to the absorption spectrum of the photosensitizer solutions before loading. Based on the standard curve created from the absorption spectra of standard MB solutions, the mass of photosensitizers incorporated into the nanoparticles can be calculated from the difference of MB absorption peaks between “before” and “after” loading.

Release Study of PS from ZnO:Er,Yb,Gd UCNPs. Ten milligrams of the prepared UCNPs-MB was soaked in 5 mL of water for different times at 37 °C, and then the mixture was centrifuged at 8000 rpm for 5 min. The supernatant was assessed by UV–visible absorbance to detect the presence of photosensitizers that leached out into the solution. The data were collected at different times (6, 12, 24, and 48 h).

Photodynamic Therapy of Cancer Cells. HepG2 cells were seeded into a 96-well cell culture plate at a seeding density of 5×10^4 cells/well and then incubated for 24 h. After cell adherent, ZnO:Er,Yb,Gd UCNPs with different concentrations (0.25, 0.5, 1, and 2 mg/mL), with and without MB loaded, were added to the wells and then the mixtures were incubated for another 12 h at 37 °C. The culture medium containing noninternalized nanoparticles was discarded and the cells were washed twice with PBS to remove any noninternalized nanoparticles and then subjected for a period of time (3–15 min) to 980-nm NIR laser irradiation with an output power of 500 mW. The cells were then incubated at 37 °C for an additional 12 h. Cell viability was measured by MTT assay as described above. Microscopy images of cells were obtained with an inverted microscope after the cells were washed with PBS and stained with 0.4% trypan blue (TB).

RESULTS AND DISCUSSION

Figure 1 shows the XRD patterns of ZnO:Er,Yb,Gd samples with different sintering temperatures in air. As is shown, when

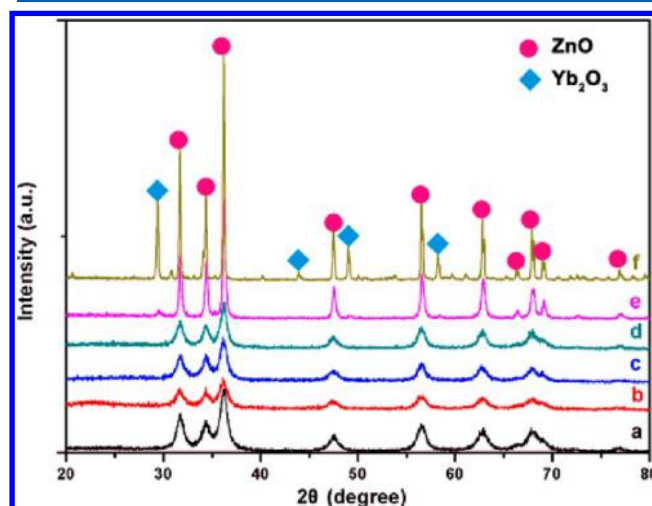


Figure 1. XRD patterns of ZnO:Er,Yb,Gd particles with varied sintering temperatures: (a) 70, (b) 700, (c) 800, (d) 900, (e) 1000, and (f) 1100 °C.

the samples were calcinated below 1000 °C, all of the diffraction peaks can be indexed and assigned to the wurtzite-structured ZnO, which were in good agreement with the theoretical values (JCPDS No. 36-1451). However, when the products were calcinated above 1000 °C, some characteristic peaks of Yb₂O₃ (JCPDS No. 88-2161) occurred. This may be due to enhanced crystallization of Yb₂O₃ at high temperatures. EDS measurements (Figure 2a) further demonstrated the existence of Zn, O, Er, Yb, and Gd in samples (Si and C signals from the slice of silicon substrate). Panels b and c of Figure 2 are TEM images of the ZnO:Er,Yb,Gd particles. The corresponding EDS elemental mappings are shown in Figure

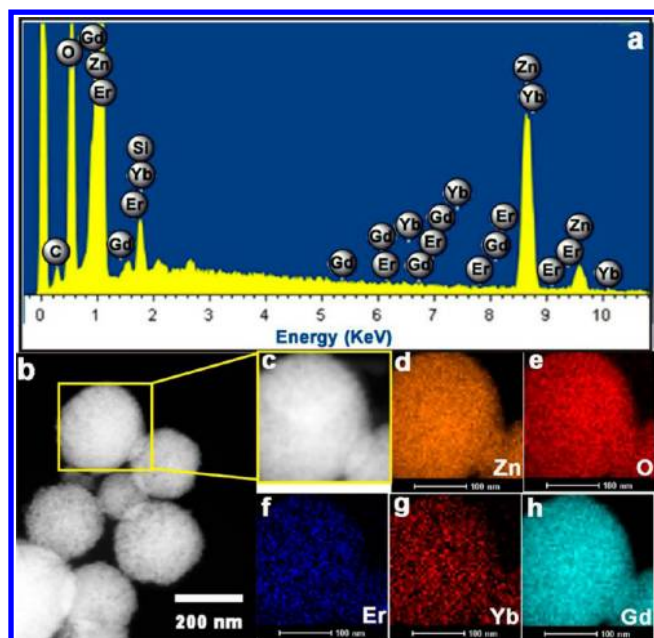


Figure 2. EDS analysis of the chemical composition distribution of the ZnO:Er,Yb,Gd particles. (a) EDS spectrum of the sample. (b) Low-magnification scanning transmission electron microscopy image of the sample. (c) Enlarged view of the region in the yellow frame in part b. (d–h) Mappings of Zn, O, Er, Yb, and Gd of the region shown in part c, respectively.

2, panels d–h, which illustrate the actual distribution of Zn, O, Er, Yb, and Gd, separately.

From the SEM images, fairly well-defined and discrete spherical shaped assemblies comprised of numerous fine nanocrystals were seen (Figure 3a,c). Each spherical assembly is made up of 3D spatially connected numerous nanocrystals of average size ~ 20 nm, which is in good agreement with the crystallite size obtained from XRD line broadening. The geometrical structure of an individual aggregate is further schematically illustrated in Figure 3b to demonstrate the structure features provided by the aggregation of nanosized crystallites. The formation of these spherically shaped particle assemblies by oriented attachment of nanocrystals during the course of the synthesis is discussed elsewhere.^{57,58} The corresponding histograms with the particle size distribution of the as-prepared particles are presented in Figure 3d and the result shows that the ZnO:Er,Yb,Gd particles have an average hydrodynamic diameter of 291 nm with relatively narrow particle size distribution. To investigate the effect of lanthanide doping on the morphology of the products, ZnO nanoparticles were synthesized via a similar method. As shown in the SEM images, ZnO:Er,Yb,Gd particles (Figure 3c) are more uniform in morphology compared with the pure ZnO (Figure S1, Supporting Information), indicating that the rare earth dopants may favor the formation of uniform ZnO nanospheres.

We further investigated the effect of sintering temperatures on the morphology of the products. From the SEM image (Figure S2a, Supporting Information) of ZnO:Er,Yb,Gd particles with a calcination temperature of 800 °C for 2 h, we can see that the particles still have spherical morphology though a few particles with smaller diameters can be observed occasionally. The corresponding size distribution measurement (Figure S2b, Supporting Information) reveals a mean particle size of 348 nm. Further increasing the calcination temperature

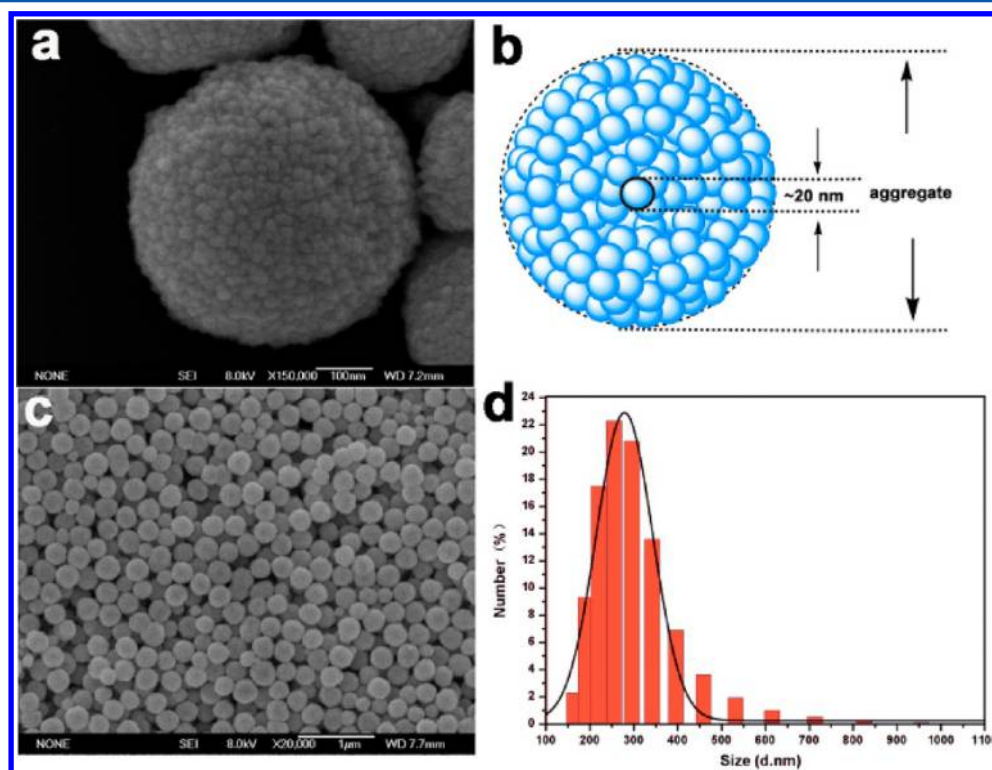


Figure 3. Morphology and structure of the ZnO:Er,Yb,Gd particles. (a) A magnified SEM image of an individual particle. (b) A schematic diagram that illustrates the microstructure of aggregated ZnO:Er,Yb,Gd comprising closely packed nanocrystallites. (c) SEM image of the samples (70 °C). (d) DLS measurement of the particle size distribution.

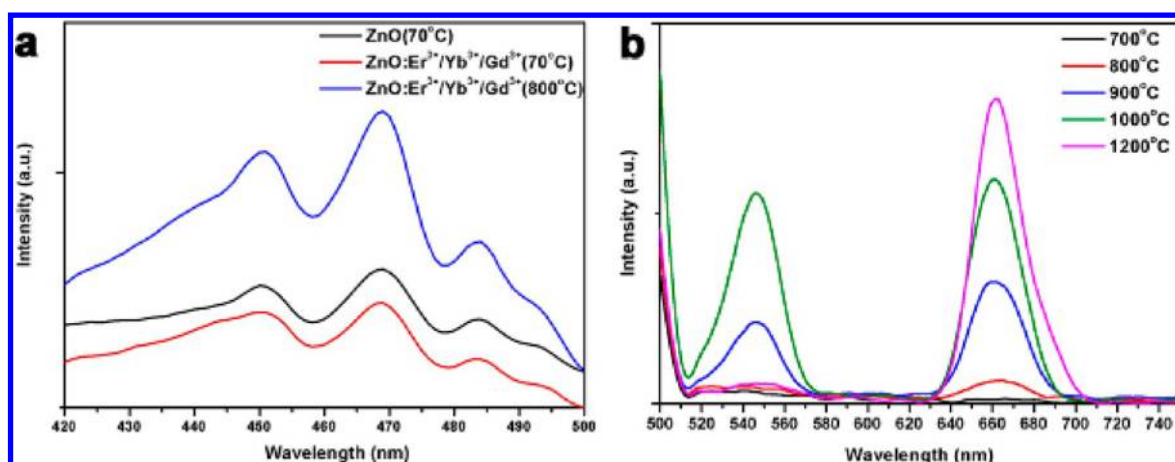


Figure 4. (a) Down-conversion ($\lambda_{\text{EX}} = 325$ nm) and (b) up-conversion ($\lambda_{\text{EX}} = 980$ nm) luminescence spectra of ZnO:Er,Yb,Gd samples with varied sintering temperatures.

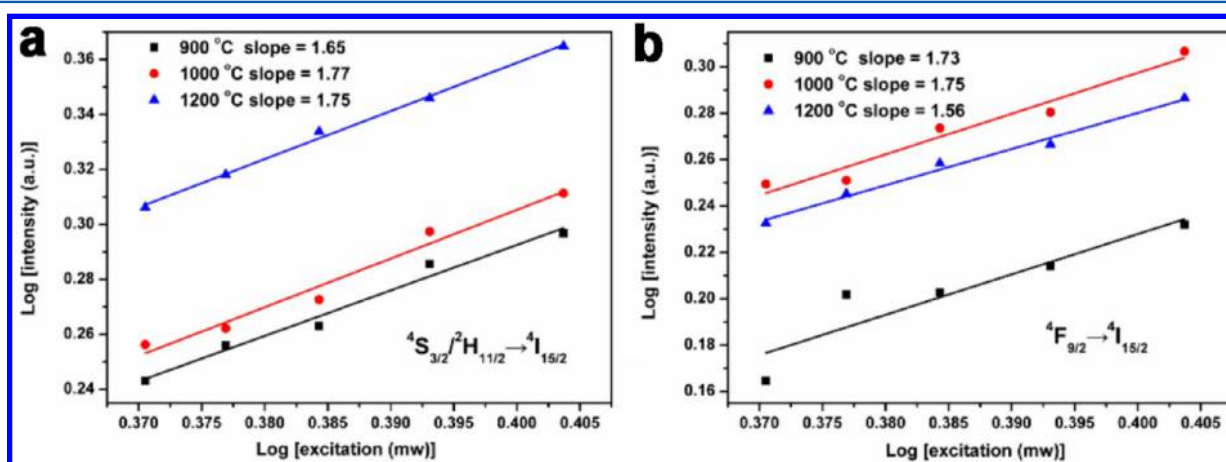


Figure 5. Double-logarithmic plots of the excitation power dependent up-conversion emission intensity of the ZnO:Er,Yb,Gd samples: (a) green up-converted emission and (b) red up-converted emission.

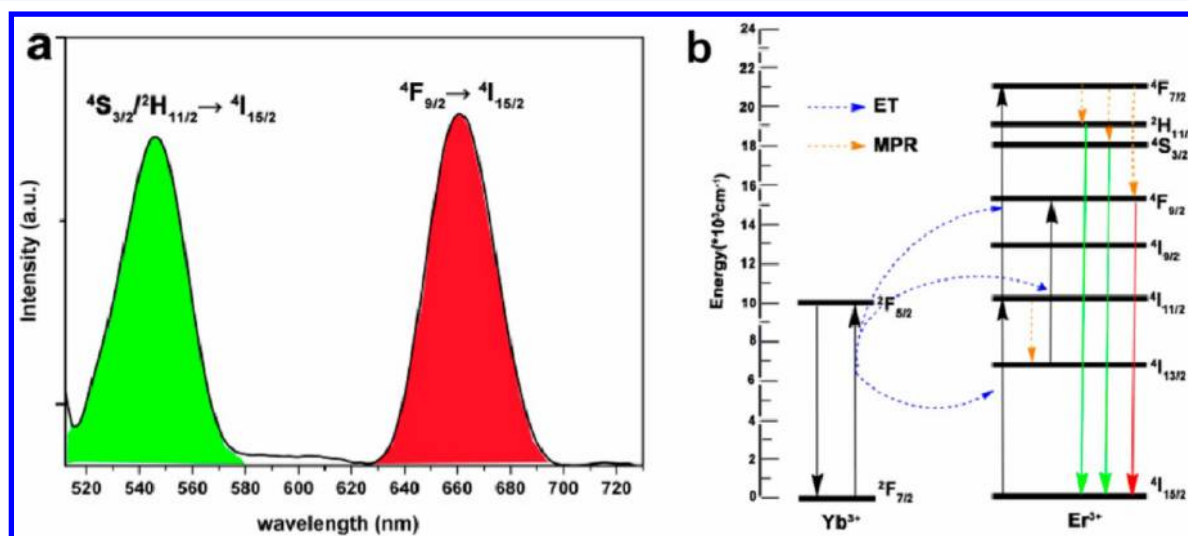


Figure 6. (a) PL spectrum of ZnO:Er,Yb,Gd samples with sintering temperature of 1000 °C ($\lambda_{\text{EX}} = 980$ nm) and (b) schematic energy-level diagrams of the Yb³⁺ and Er³⁺ ions in samples and the up-conversion mechanism excited by a 980 nm diode laser.

may lead to larger particle size and less uniformity of ZnO:Er,Yb,Gd particles. The sample calcinated at 1000 °C presents worse dispersity with an enhanced mean particle size of 920 nm (Figure S3, Supporting Information). In addition,

through the statistical analysis of their SEM images, the size distributions of ZnO:Er,Yb,Gd particles sintered at 70 and 800 °C with average diameters of ~ 270 and ~ 327 nm are monomodal (Figure S4, Supporting Information), which are

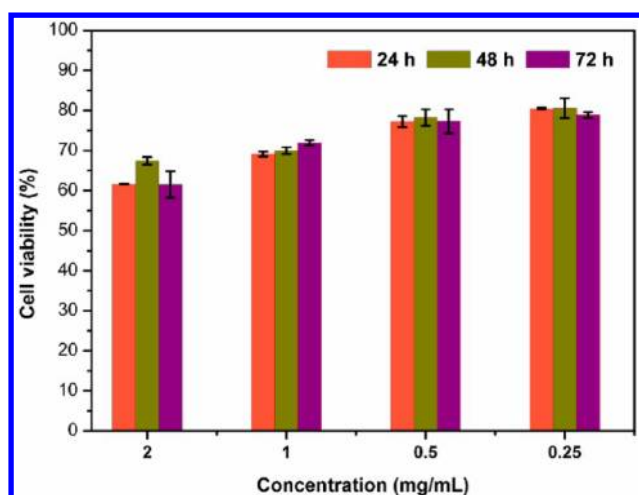


Figure 7. Cell viabilities of HepG2 cells incubated with various concentrations of ZnO:Er,Yb,Gd particles for different times.

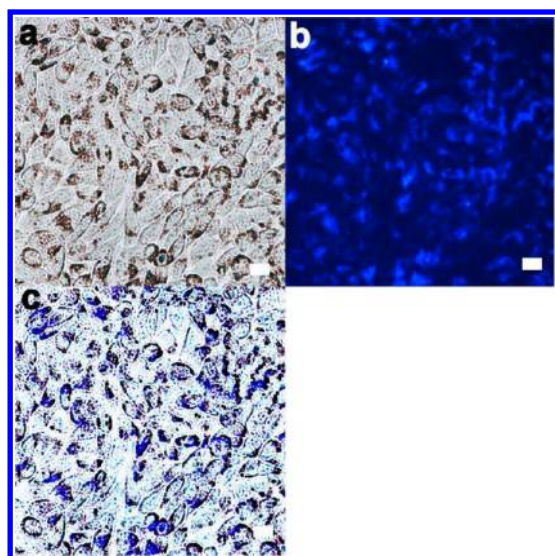


Figure 8. Optical microscopy images of HepG2 cells incubated with ZnO:Er,Yb,Gd particles: (a) phase contrast image, (b) fluorescence image, and (c) overlay of fluorescence and phase contrast images. Scale bars = 20 μm .

smaller than the results of DLS (291 and 348 nm, respectively). This may be due to the hydrated layer on the surface of particles as DLS was conducted by dispersed water-soluble samples in ultrapure water. The particles can be easily dispersed in ultrapure water and formed a stable aqueous suspension for ~ 40 h at room temperature (Figure S5a, Supporting Information). The corresponding DLS measurements of the ZnO:Er,Yb,Gd sample in ultrapure water with different standing time (Figure S5b, Supporting Information) further demonstrate the size change of particles with the standing time. As can be seen from Figure S5b, Supporting Information, the average size of particles was gradually increased from 348 to 469 nm after 12 h; a microstructure of aggregated ZnO:Er,Yb,Gd may be formed within this period, because the particles would have collided with each other to form few aggregated structures and finally precipitated at the bottom after standing 40 h, which could be observed from Figure S5a, Supporting Information. However, the particles size remains at

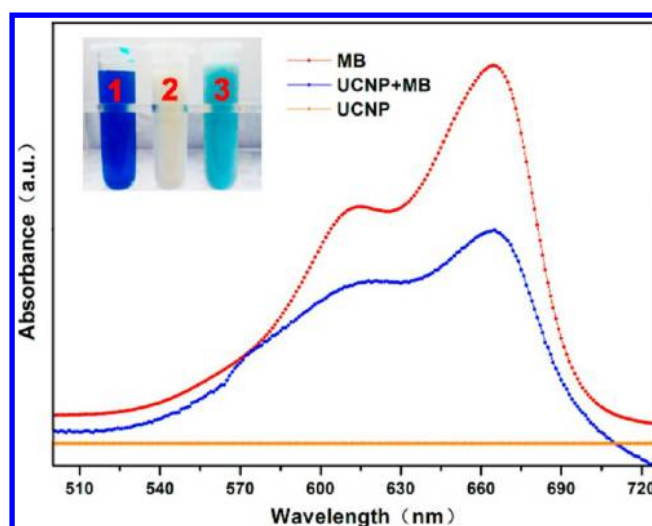


Figure 9. UV/vis absorption spectra of MB, ZnO:Er,Yb,Gd and ZnO:Er,Yb,Gd-MB particles. The inset shows digital photos of MB (left, 1), ZnO:Er,Yb,Gd (middle, 2) and ZnO:Er,Yb,Gd-MB particles (right, 3) in deionized water under natural light.

~ 234 nm with standing time of 40 h, which would be beneficial for the particle cellular interaction.

To determine the capacity of these ZnO:Er,Yb,Gd nano-assemblies for the uptake of gases/foreign molecules, such as drugs, we measured the N_2 adsorption–desorption isotherm. The surface area calculations were carried out by using the BET method. As seen from Figure S6, Supporting Information, the prepared ZnO:Er,Yb,Gd products exhibited a hysteresis loop at high relative pressure, suggesting their multiporous structure. This structure could be attributed to the interspaces between the assembled nanoparticles, in accordance with the microscopy results (inset of Figure S6, Supporting Information). The results show that the BET surface area of the ZnO:Er,Yb,Gd particles with a calcination temperature of 70 $^\circ\text{C}$ was 36.65 $\text{m}^2 \text{g}^{-1}$, which was larger than that (5.23 $\text{m}^2 \text{g}^{-1}$) with a calcination temperature of 800 $^\circ\text{C}$. This may be caused by the lattice expansion and collapse of interspaces between nanoparticles of ZnO:Er,Yb,Gd sample through calcination.

The room temperature down-conversion photoluminescence (PL) properties of the samples obtained at different sintering temperatures were investigated by using a 325 nm Xe laser as the excitation source (Figure 4a). From the PL spectra, it can be seen that the pure ZnO and the ZnO:Er,Yb,Gd particles sintered at 70 $^\circ\text{C}$ exhibit similar emission peaks, including a violet band (450 nm) and a blue band (468 nm), which are attributed to the transition from Zn_i and extended Zn_i states to the valence band, respectively.⁵⁹ For the ZnO:Er,Yb,Gd particles sintered at 800 $^\circ\text{C}$, the intensity of down-conversion luminescence was enhanced significantly.

As is well-known, Er^{3+} ions are excellent dopants and have the capability of converting infrared radiation to visible light efficiently because of favorable electronic energy levels (such as $^4\text{I}_{9/2}$ and $^4\text{I}_{11/2}$) that are easily accessible with NIR radiation. Furthermore, the low phonon-energy and appropriate coordination of impurities around Er makes ZnO suitable for the realization of efficient upconversion luminescence.⁶⁰ The up-conversion luminescence spectra of the products were measured by using a spectrophotometer under the excitation of an unfocused 980 nm laser diode at room temperature. Because no obvious up-conversion luminescence of ZnO:Er,-

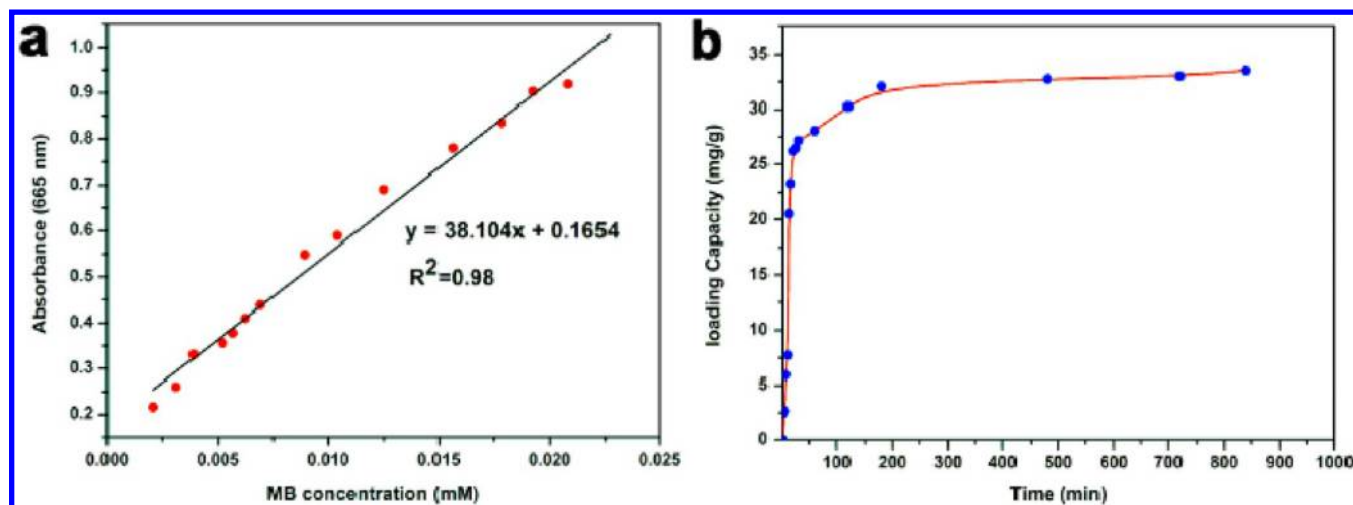


Figure 10. (a) Linear calibration plot between the absorbance at 665 nm and concentration of MB. (b) Time-dependent MB loading capacity of ZnO:Er,Yb,Gd UCNPs.

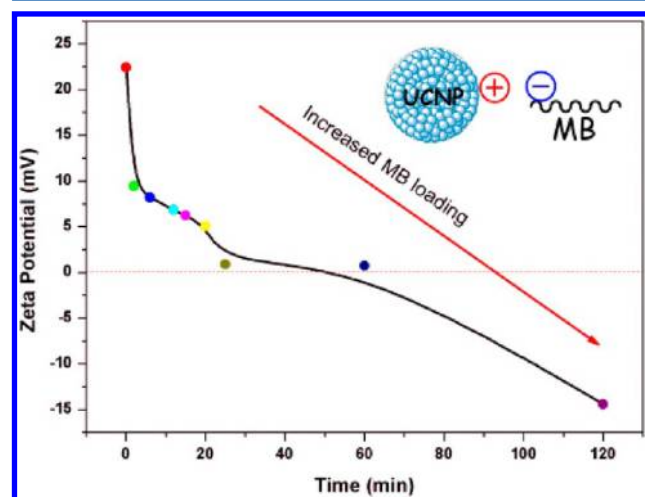


Figure 11. The change of ζ potentials of UCNPs-MB in ultrapure water for different periods of time. The inset drawing shows the Coulombic force between MB and ZnO:Er,Yb,Gd nanoparticles.

Yb,Gd particles can be detected at low temperatures ($<700^\circ\text{C}$) in this system (data not shown here), calcination at high temperatures was necessary. Figure 4b shows the up-conversion luminescence spectra of samples with varied sintering temperatures. According to previous reports,^{61,62} the green emission band centered at 545 nm is attributed to the $^4\text{S}_{3/2}/^2\text{H}_{11/2} \rightarrow ^4\text{I}_{15/2}$ electronic transition of the Er^{3+} ions. On the other hand, the 662 nm red emission is ascribed to the $^4\text{F}_{9/2} \rightarrow ^4\text{I}_{15/2}$ transition of Er^{3+} ions. Here, the role of Yb^{3+} is sensitizer. The sensitization of Yb^{3+} ions can improve the conversion efficiency of Er^{3+} ions significantly. This is because Yb^{3+} ions have large absorption cross section near a wavelength of 980 nm and they can transfer the excitation energy to the Er^{3+} ions nearby through resonance.⁶³ From Figure 4b, it can be seen that the intensity of the green emission band increased gradually with the rising of sintering temperature. This may be related to the concentration of defects in the samples. As we know, the higher the temperature, the higher the concentration of defects. And the defects can form luminescence centers which can enhance optical properties of samples.⁶⁴ We further investigated the effect of doping ratio on the optical properties of the samples,

and results have shown that the prepared $\text{ZnO}_{0.85}\text{Er}_{0.02}\text{Yb}_{0.1}\text{Gd}_{0.03}$ samples have better up-conversion luminescence properties than other products with different doping ratios (Figure S7, Supporting Information).

Herein, we conducted a preliminary discussion on the fluorescence mechanism of the prepared ZnO:Er,Yb,Gd particles. It is known that an important factor that governs the upconversion efficiency is the nonradiative relaxation rate (W_{nr}) and it is dependent upon the energy gap (ΔE) separating the upper and lower states as well as the highest phonon energy in the material. The number of phonons (P_{phonons}) required to complement the ΔE can be calculated according to eq 1, where $h\omega$ is the energy of the phonons in the surrounding medium. The relationship between W_{nr} and P_{phonons} can be determined through eq 2, where both C and α are constants. In addition, the fluorescence quantum yield (η) is related to the radiative and the nonradiative recombination rates, W_{r} and W_{nr} , expressed by eq 3.

$$P_{\text{phonons}} = \Delta E/h\omega \quad (1)$$

$$W_{\text{nr}} = C \exp(-\alpha P_{\text{phonons}}) \quad (2)$$

$$\eta = W_{\text{r}}/(W_{\text{r}} + W_{\text{nr}}) \quad (3)$$

For the prepared ZnO:Er,Yb,Gd particles, there may be some residual organics (such as alcohol and DEG) and H_2O present in the particles. And the presence of the high-frequency vibration modes of some functional groups such as $\text{C}=\text{O}$, $\text{H}-\text{O}$ can consume the P_{phonons} , which matches the gap of the two energy levels. Thus, no distinct emission bands of Er^{3+} can be detected when calcinated at low temperatures. With the increase of sintering temperature, The amount of high-frequency groups on the ZnO:Er,Yb,Gd surface decreased, leading to the relative increase of P_{phonons} and decrease of W_{nr} . Consequently, the η would increase.^{60,65} Thus emission bands of Er ions can only be detected after the samples were calcinated at high temperatures. This is consistent with our experimental results. As shown in the FTIR spectra (Figure S8, Supporting Information), the vibration intensities of residual organic groups and H_2O in ZnO:Er,Yb,Gd particles decreased with the annealing temperature increasing from 70 to 800 $^\circ\text{C}$.

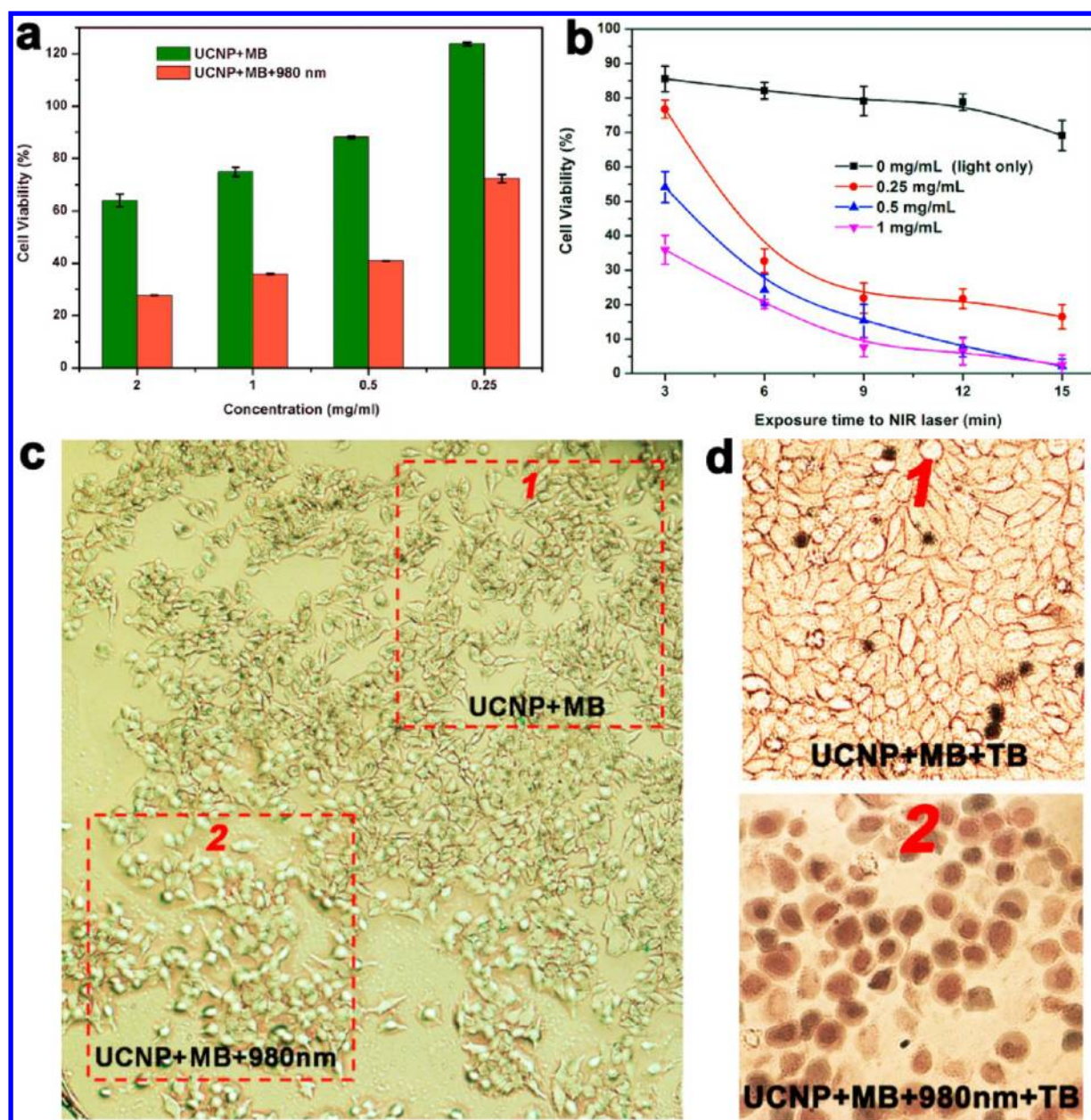


Figure 12. (a, b) Cell viability data of HepG2 cells after various treatments indicated as evaluated by the standard MTT assay. (c) Optical microscopy image of HepG2 cells incubated with ZnO:Er,Yb,Gd-MB particles for 12 h (zone 1) and further exposed to NIR laser for a period of time (zone 2). (d) The corresponding TB stained cells image of part c.

To further reveal the up-conversion mechanism, the excitation power dependence of the green and red emissions was investigated. The up-conversion emission intensity (I_{up}) can be determined by using the following equation:⁶⁶

$$I_{up} \propto P_{power}^N \quad (4)$$

where I_{up} is the luminescence intensity, P_{power} is the excitation power, and N is the number of photons required to produce one up-conversion emission photon and can be determined by the slope of the fitted line of the plot of $\log(I_{up})$ versus $\log(P_{power})$. As shown in Figure 5, all the N values are approximately equal to 2, indicating that two photons are involved in the up-conversion process for all emission bands.

The suggested mechanism responsible for the up-conversion luminescence of the Yb^{3+} – Er^{3+} couples is shown in Figure 6b. When the samples are excited with a 980 nm diode laser, a Yb^{3+}

ion absorbs the energy of a 980 nm photon, and then an energy transfer from the Yb^{3+} ion in the $^2F_{5/2}$ level to the ground state of the Er^{3+} leads to the $^4I_{15/2} \rightarrow ^4I_{11/2}$ transition of Er^{3+} . Simultaneously, the $^4I_{13/2}$ level of Er^{3+} is generated with a process of multiphonon relaxation (MPR). The following twice energy transformation (ET) from $^2F_{5/2}$ of Yb^{3+} to the $^4I_{13/2}$ and $^4I_{9/2}$ levels of Er^{3+} occurs and makes the Er^{3+} ions transfer to higher levels ($^4F_{7/2}$ and $^4F_{9/2}$ levels, respectively). The $^4S_{3/2}/^2H_{11/2}$ and $^4F_{9/2}$ levels are subsequently generated with the process of MPR. Lastly, the green and red emissions are obtained with the electronic transition of $^4S_{3/2}/^2H_{11/2} \rightarrow ^4I_{15/2}$ and $^4F_{9/2} \rightarrow ^4I_{15/2}$, respectively.^{67,68} The corresponding PL spectrum of these two electronic transitions was shown in Figure 6a.

The near-IR luminescence of prepared samples is a special benefit for biological applications because (i) there is an

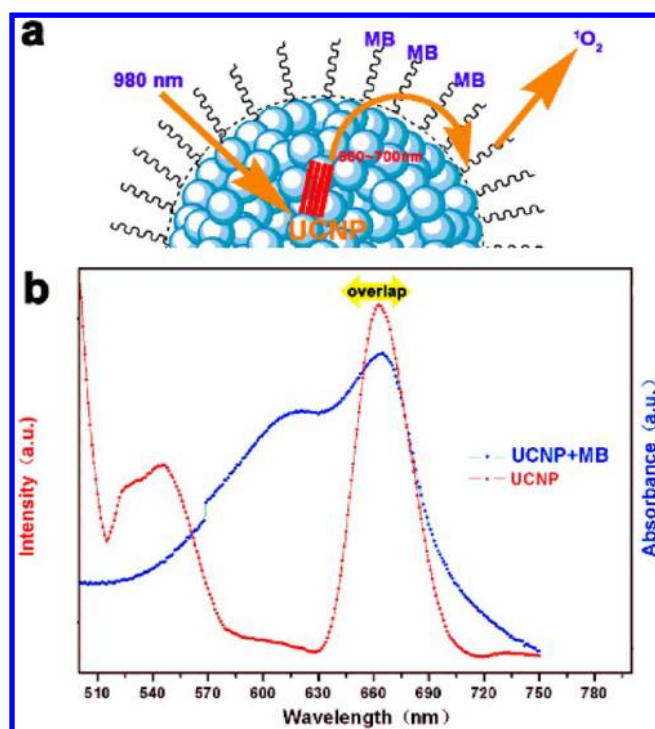


Figure 13. (a) Schematic illustration showing how PDT works using UCNP-MB. On exposure to NIR light, the nanoparticles convert NIR light to visible light, which will activate the MB to produce reactive oxygen species to kill cancer cells. (b) Overlap between ZnO:Er,Yb,Gd-MB absorption and ZnO:Er,Yb,Gd UCNP's emission: red-band emission of up-conversion fluorescence spectrum of ZnO:Er,Yb,Gd under NIR laser excitation (red line); UV/vis absorption spectrum of ZnO:Er,Yb,Gd-MB in water located at 665 nm (blue line).

absence of native autofluorescence of tissues in the near-IR region and, therefore, a good signal-to-noise ratio is obtained for more sensitive detection, and (ii) near-IR photons can cross significant depths of tissues for potential noninvasive investigation.¹⁶

The leaching experiment was conducted by ICP analysis after incubating the ZnO:Er,Yb,Gd particles in the PBS for one month. The result (data not shown here) displayed that no rare earth ion was detected in the supernatant after centrifugation separation, revealing the stability of our samples in a physiological environment. Figure S9 in the Supporting Information shows the XRD pattern of products which were soaked in the PBS for one month and it was in good agreement with the wurtzite-structured ZnO (JCPDS NO. 36-1451), indicating that the particles remained in a desirable structure after being incubated in PBS for a long time. The good stability of the ZnO:Er,Yb,Gd particles allows us to further use it for various biological applications.

Generally, the actual biological application of samples needs to address the question about its biocompatibility. Low or no cytotoxicity is one of the most critical parameters for ideal biomaterials. To evaluate the cytotoxicity of the as-prepared sample, we used the MTT assay method to measure the relative cell viability. This method was widely used to measure the mitochondria activity to quantify the cell death. The data shown in Figure 7 demonstrated that the cell viability was not significantly affected by incubation in the presence of the prepared particles where the viabilities remain at 60–70% even at high concentrations of 2 mg/mL. With a fixed products

concentration of 2 mg/mL, the cell viability was high and remains above 60% during the first 24 h and still as high as 60% even after 72 h of incubation, indicating favorable biocompatibility of the products.

The favorable data obtained above make interesting candidates for cellular imaging. Optical microscopy images of HepG2 cells incubated with ZnO:Er,Yb,Gd nanoparticles were next collected with use of an inverted microscope. As shown in Figure 8, the HepG2 cells show distinct blue fluorescence under UV radiation, which is consistent with the down-conversion photoluminescence mentioned above, indicating that the ZnO:Er,Yb,Gd nanoparticles are internalized by the cells and could be used as effective labeling probes.

Nanoparticles uptake into cells could go through different processes including phagocytosis, fluid-phase, endocytosis, and receptor-mediated endocytosis.⁶⁹ Many investigations have shown that these operations are performed simultaneously, but the main role is endocytosis, which contains two processes: (1) the sample attached to the cell membrane and is surrounded by a small capsule which formed due to the invagination of membrane and (2) vesicles which formed by the small pouch separated from cell membrane enter into the interior of the cell.^{70–72} This mechanism is true for the cellular uptake of ZnO:Er,Yb,Gd nanoparticles as the results have shown that these samples have good biocompatibility. In addition, FBS which contains many serum proteins was used when HepG2 cells were incubated with ZnO:Er,Yb,Gd nanoparticles in our experiment. Among these serum proteins, transferrin is such a suitable “ligand” for conjugating particles, since it can be specifically recognized and taken up by transferrin receptors actively expressed on the surface of tumor cells.^{73,74} The transferrin–receptor interaction has therefore been exploited as a potential efficient pathway for the cellular uptake of nanoparticles and drugs. Thus, the transferrin absorption on the surface of the prepared particles during incubation may promote the endocytosis process of HepG2 cells for ZnO:Er,Yb,Gd nanoparticles. The results of FTIR (Figure S10, Supporting Information) have shown that there are abundant hydrophilic groups (especially the hydroxyls, O–H) in ZnO:Er,Yb,Gd particles as the products were prepared in the solution of DEG, these functional groups are favorable for the nanoparticles uptake into cells. Compared with the sample free of FBS (black line, Figure S10, Supporting Information), more functional groups such as C–N, N–H groups are found in the ZnO:Er,Yb,Gd particles incubated with FBS (red line, Figure S10, Supporting Information). This result indicates that the protein and ZnO:Er,Yb,Gd nanoparticles were effectively combined, which further promotes the phagocytosis of cells. Furthermore, studies have shown that many cell types can actively ingest microspheres and the ideal size of microspheres for this purpose ranges from about 0.5 to 2 μm .^{75,76} The HepG2 cell is one of the cell types that can actively ingest microspheres; Wei and colleagues⁷⁷ have studied the phagocytosis of HepG2 cells using chitosan microspheres with a diameter of 1.9 μm , and the results have shown that these microspheres with autofluorescence could be used as novel tracers.

Based on the study above, we developed a kind of UCNP/MB-based PDT drug by using ZnO:Er,Yb,Gd UCNP's and water-soluble MB. The inset of Figure 9 shows photographs of MB, ZnO:Er,Yb,Gd, and ZnO:Er,Yb,Gd-MB particles dispersed in water under ambient light. Relative to typical milk-white-colored non-MB-loaded ZnO:Er,Yb,Gd UCNP's solution, a

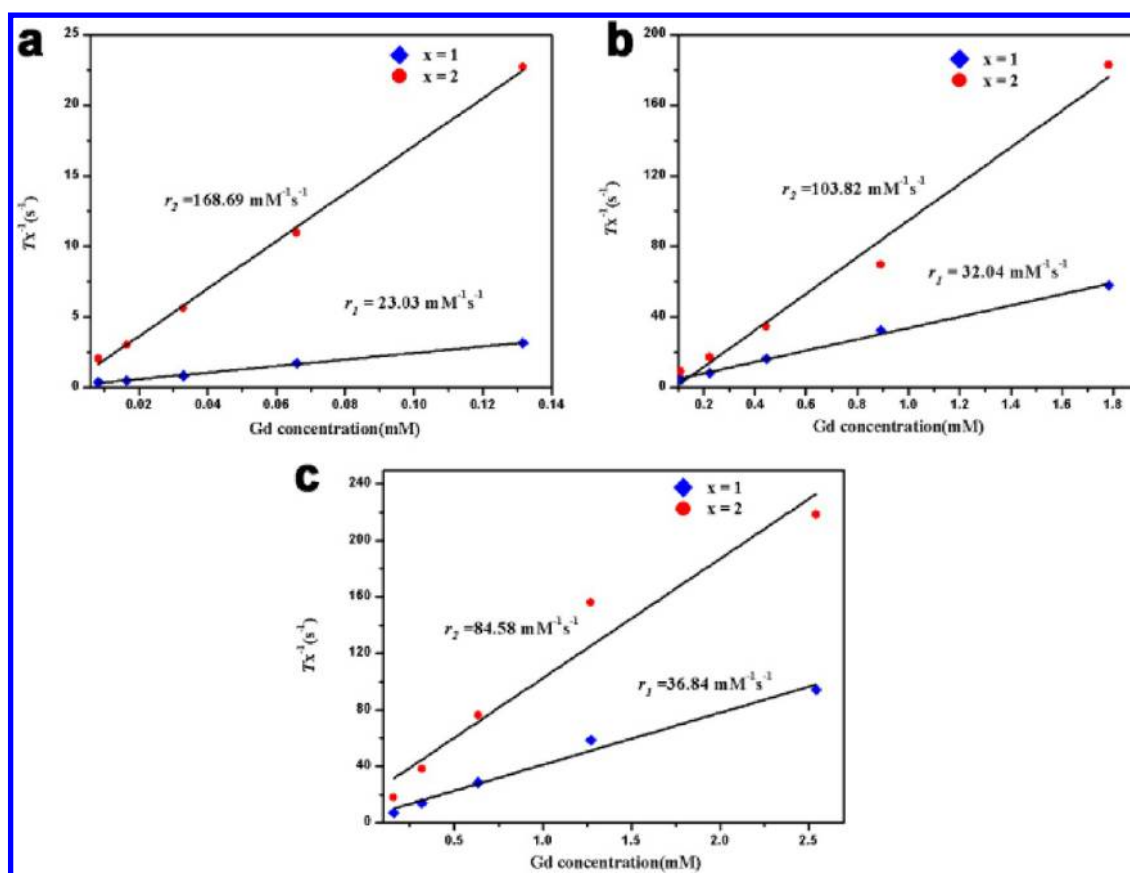


Figure 14. The linear relationship between T_x relaxation rates ($x = 1, 2$) and Gd^{3+} ion concentrations of ZnO:Er,Yb,Gd particles with varied doping ratios of Gd^{3+} ions: (a) 1% Gd^{3+} , (b) 2% Gd^{3+} , and (c) 3% Gd^{3+} .

clearly cyan-colored water solution could be seen for ZnO:Er,Yb,Gd-MB, thereby clearly demonstrating the successful loading of MB onto the particles. The UV/vis spectrum provides more convincing evidence with remarkable MB absorption peaks located at 665 nm in the ZnO:Er,Yb,Gd-MB sample, whereas no such peaks could be found in pure ZnO:Er,Yb,Gd UCNP, as seen in Figure 9.

A standard curve method was performed to obtain the calibration curve of the absorbance at 665 nm against MB concentration (Figure 10a), and the loading capacity of MB in ZnO:Er,Yb,Gd UCNP was further investigated according to it. As shown in Figure 10b, the adsorption process was carried out quickly within the first 100 min; after 3 h, the adsorption capacity of UCNP remained almost unchanged, indicating that the MB adsorption reaction has reached equilibrium. The value of the maximum MB adsorption capacity of ZnO:Er,Yb,Gd UCNP is about 33 mg/g. To evaluate the stability of MB loading on the UCNP, a release study of the photosensitizers from the UCNP was performed. Absorbance readings at 665 nm from the supernatant of ZnO:Er,Yb,Gd-MB soaked in water for different times were used to detect the release of MB. It has been observed from Figure S11 in the Supporting Information that the release of MB attained a plateau after 12 h, and the amount of release was low compared to that of the initial products, which shows the good stability of prepared UCNP-MB.

In the time-dependent ζ potentials changing study (Figure 11), obvious charge conversion, with the nanoparticles ζ potential decreasing from around +22 to -15 mV in a period of 2 h, was observed, which indicates that one of the main binding

forces between MB and ZnO:Er,Yb,Gd nanoparticles is the Coulombic force between negative charge and positive charge on the surface of MB and UCNP, respectively (inset of Figure 11).

The in vitro PDT effects of the ZnO:Er,Yb,Gd-MB particles were assessed by cell viability. After incubation with different concentrations of ZnO:Er,Yb,Gd-MB for 12 h, the HepG2 cells were irradiated with NIR light for 3 min and incubated for an additional 12 h. Compared to the control group without NIR light irradiation, the cell viability in the NIR light irradiated groups decreased dramatically with an increase in the concentration of ZnO:Er,Yb,Gd-MB samples (Figure 12a). To confirm the PDT effects induced by MB, the cells were incubated with non-MB-loaded ZnO:Er,Yb,Gd particles as controls. The results (Figure S12, Supporting Information) indicate that for non-MB-loaded ZnO:Er,Yb,Gd particles, the discrepancy in cell viability with and without 980 nm irradiation is much smaller than that for ZnO:Er,Yb,Gd-MB particles ($\sim 15\%$ vs $\sim 50\%$). This small decrease in cell viability may be due to a little thermal therapy effect caused by NIR light.³⁶ The PDT effects of the products for the different exposure times (3, 6, 9, 12, and 15 min) to the NIR laser with varied concentrations of UCNP-MB (0, 0.25, and 0.5, 1 mg/mL) were further evaluated. To avoid the heating of cell culture induced by the 980 nm laser in the long period of the light exposure process, the laser was switched off after each 3 min of irradiation, and then switched on after another 3 min interval (to let the cell culture cool). As shown in Figure 12b, the cancer cell killing efficacy is more obvious even at the low UCNP-MB concentration of 0.25 mg/mL. A cell without UCNP-MB but

with laser exposure only was induced as the control, and the result (Figure 12b, black line) shows a small decrease ($\sim 10\%$) in cell viability even at the long exposure time of 15 min. Figure 12c demonstrates the differences in HepG2 cell morphology with (zone 2) and without (zone 1) NIR light irradiation. As is shown, the incubation with ZnO:Er,Yb,Gd-MB for 12 h did not cause significant changes on the cells (zone 1); however, after a further exposure to the 980 nm laser for a period of time the cell morphology was notably changed and obvious cell apoptosis can be observed (zone 2). To differentiate the dead and live cells, trypan blue (TB), which can detect the integrity of the cell membrane, was used to stain the dead cells. Figure 12d further demonstrates the NIR induced PDT effects of ZnO:Er,Yb,Gd-MB UCNPs. These results suggest that the death of cells is dominated by the PDT effect of MB activated by the ZnO:Er,Yb,Gd UCNPs. Due to the deep tissue penetration of NIR light, ZnO:Er,Yb,Gd-MB particles possess great potential for in vivo PDT of cancer.

As we know that PDT is effective in the induction of cell death through cytotoxic reactive oxygen species (ROS), which is generated by energy transfer from the excited photosensitizers to surrounding oxygen,^{41–46} it is commonly considered that singlet oxygen ($^1\text{O}_2$) is primarily responsible for inducing cell death.^{78,79} The excitation light of UCNPs is in the NIR region, which is a transparent window in the tissue and permits deeper tissue penetration than visible light.⁸⁰ The emission light from the excited UCNPs is in the visible region, which overlaps the excitation range of some PS. In principle, when the PS is close enough to UCNP, the smaller the wavelength mismatch between PS absorption and UCNP emission is, the higher the $^1\text{O}_2$ generation efficiencies will be.⁸¹ Due to its well-matched absorption (665 nm) with ZnO:Er,Yb,Gd UCNPs emission (662 nm), MB is selected as PS in our study. MB has been actively used in the microbiological and pharmacological fields before being considered as a drug for NIR laser triggered PDT.^{83,84} The quantum yield of $^1\text{O}_2$ generation of MB is high and it has almost negligible dark toxicity.^{85,86} Figure 13b clearly shows the spectra overlap between MB absorption and the ZnO:Er,Yb,Gd red emission peak with an absorption/emission mismatch estimated to be less than 5 nm.

The Gd^{3+} ions in the ZnO:Er,Yb,Gd particles can accelerate longitudinal (T_1) relaxation of water protons and exert bright contrast in regions where the nanoprobe localizes. To evaluate the MRI contrast efficiency of the as-prepared products, we measured the longitudinal relaxation time (T_1) and transverse relaxation time (T_2) of their aqueous solutions at clinical field strength (1.5 T) with physiological temperature (37 °C) to investigate whether the sample can serve as a T_1 contrast agent. The inverse relaxation times as a function of the Gd molar concentrations are shown in Figure 14. Then, the nuclear longitudinal relaxivity r_1 and transverse relaxivity r_2 , which represent the efficiency of the magnetic nanoparticles as a contrast agent shortening the proton relaxation times, were determined by calculating the slope of a plot of the inverse relaxation time against the Gd concentrations. As shown in Figure 14, the values of r_1 of the ZnO:Er,Yb,Gd particles doped with 1%, 2%, and 3% Gd^{3+} ions are 23.03, 32.04, and 36.84 $\text{mM}^{-1} \text{s}^{-1}$, while the values of r_2 are 168.69, 103.82, and 84.58 $\text{mM}^{-1} \text{s}^{-1}$, respectively. Thus the ratio of r_2/r_1 can be modified in a wide range from 7.32 to 2.29 with increasing the Gd^{3+} doping content from 1% to 3% in ZnO:Er,Yb,Gd particles. Notably, the resulting r_1 values are much larger than the

commercially available Gd-DTPA ($r_1 = 4.5 \text{ mM}^{-1} \text{s}^{-1}$),⁸⁷ Gd-doped ZnO quantum dots ($r_1 = 16 \text{ mM}^{-1} \text{s}^{-1}$).²⁶ The results suggest the sample is an ideal candidate for T_1 imaging at clinical field strength.

Herein, we further researched the reason of the enhancement of r_1 values of the synthesized particles compared with the Gd-DTPA and Gd-doped ZnO quantum dots, etc. In general, the T_1 contrast effect is induced by the interactions between protons of water molecules and electron spins of the contrast agents and the T_1 relaxivity (r_1) can be determined through the eq 5, in which C is a constant, q is the number of inner sphere water molecules, μ_{eff} is the effective magnetic moment, τ_c is the molecular correlation time, and r is the Gd–H (H_2O) distance.^{88,89} Among them, rotational correlation time τ_r is one of the parameters that can influence the τ_c (eq 6). Research has shown that changing molecular size is one of the possible approaches to increase τ_r , which can lead to dramatic increases in r_1 .⁹⁰ For example, protein-bound Gd-DTPA has relaxivities approaching 20 $\text{mM}^{-1} \text{s}^{-1}$, compared to 4 $\text{mM}^{-1} \text{s}^{-1}$ for the chelate alone. In our study, the sizes of prepared ZnO:Er,Yb,Gd particles are larger than those of Gd-DTPA and the Gd-doped ZnO quantum dots and have the larger values of τ_r , so the r_1 values for them are much larger than those for Gd-DTPA and the Gd-doped ZnO quantum dots. According to the Solomon–Bloembergen–Morgan theory, the paramagnetic relaxation enhancement of gadolinium chelates originates from two mechanisms: the inner-sphere (IS) and outer-sphere (OS) mechanisms.⁹¹ An inner-sphere proton relaxation mechanism involves bonding of water molecules directly to Gd^{3+} ions, while no water to Gd^{3+} ion bonding is needed for an outersphere relaxation mechanism. The overall longitudinal relaxivity is the sum of inner-sphere relaxivity, r_1^{IS} , and outersphere relaxivity, r_1^{OS} . Studies have shown that the number of coordinated water molecules in the first coordination sphere is one of the most structure-related parameters for r_1^{IS} optimization, and the larger the number, the larger the r_1 .⁹² In addition, for nanoparticle-based contrast agents, a porous matrix has been commonly reported to be a better choice than a dense one because of the relatively greater accessibility of water molecules.^{93,94} In our study, the prepared ZnO:Er,Yb,Gd were porous particles, which is useful for improving the r_1 values of nanoparticles.

$$r_1 = Cq\mu_{\text{eff}}^2\tau_c r^{-6} \quad (5)$$

$$\tau_c^{-1} \propto \tau_r^{-1} \quad (6)$$

CONCLUSION

In summary, our work demonstrates a facile approach to obtain bifunctional magnetic-optical ZnO:Er,Yb,Gd particles. The XRD and SEM analysis reveals that the samples have pure wurtzite structure with uniform spherical morphology. The down-conversion luminescence of products can be obtained by using a 325 nm Xe laser as the excitation source. Under the excitation of a 980 nm laser diode, the ZnO:Er,Yb,Gd particles emit up-conversion fluorescence, which is beneficial for in vivo biomedical applications due to the increased penetration depth and low radiation damage of NIR light in biotissues. The cytotoxicity assay with HepG2 cells revealed the low toxicity of the products even at a high concentration of 2 mg/mL. Successful fluorescent labeling of HepG2 cells was accomplished by the nanoparticles. In MRI studies, ZnO:Er,Yb,Gd

particles demonstrate a tunable r_1 from 23.03 to 36.84 $\text{mM}^{-1} \text{s}^{-1}$, which are much larger than the conventional Gd-DTPA and currently reported Gd-base nanoparticles, suggest they would be a good candidates as MRI agents. In addition, the ZnO:Er,Yb,Gd particles can serve as nanotransducers in NIR triggered PDT treatment to activate the well-selected photosensitizer of MB and kill the HepG2 cells effectively. All the results demonstrate the promising potential of using ZnO:Er,Yb,Gd UCNP as the agents in magnetic-fluorescent bimodal imaging and new photosensitizer carriers for PDT of cancer in deep tissues.

■ ASSOCIATED CONTENT

■ Supporting Information

SEM image of the prepared ZnO particles (Figure S1), SEM image and DLS measurement of the ZnO:Er,Yb,Gd sample with calcination temperature of 800 °C for 2 h (Figure S2), SEM image and DLS measurement of the ZnO:Er,Yb,Gd sample with calcination temperature of 1000 °C for 2 h (Figure S3), particles size distribution and the corresponding SEM images of the as-prepared samples with different calcination temperatures (Figure S4), digital photos of ZnO:Er,Yb,Gd particles in ultrapure water under natural light with different standing time and the corresponding DLS measurement of the ZnO:Er,Yb,Gd sample with different standing times (Figure S5), N_2 adsorption-desorption isotherms of ZnO:Er,Yb,Gd particles with varied sintering temperatures (Figure S6), PL spectra of ZnO:Er,Yb,Gd samples with varied doping ratios of Er^{3+} and Yb^{3+} ions (Figure S7), FTIR spectra of the ZnO:Er,Yb,Gd samples with varied sintering temperatures (Figure S8), XRD spectrum of the ZnO:Er,Yb,Gd sample soaked in PBS for one month (Figure S9), FTIR spectra of the ZnO:Er,Yb,Gd samples before and after adding FBS (Figure S10), UV/Vis absorption spectra of ZnO:Er,Yb,Gd-MB in water and the supernatants for different times (Figure S11), and cell viabilities of HepG2 cells incubated with non-MB-containing ZnO:Er,Yb,Gd UNCPs at different concentrations (Figure S12). This material is available free of charge via the Internet at <http://pubs.acs.org>.

■ AUTHOR INFORMATION

Corresponding Author

* E-mail: kchen@qust.edu.cn. Fax: 86 532 84022509.

Notes

Notes. The authors declare no competing financial interest.

■ ACKNOWLEDGMENTS

This research was financially supported by the National Natural Science Foundation of China (Grant No. 51072087), Natural Science Foundation of Shandong Province (BS2012CL015), and Specialized Research Fund for the Doctoral Program of Higher Education (20113719110001).

■ REFERENCES

- (1) Gao, X.; Cui, Y.; Levenson, R. M.; Chung, L. W. K.; Nie, S. In Vivo Cancer Targeting and Imaging with Semiconductor Quantum Dots. *Nat. Biotechnol.* **2004**, *22*, 969–976.
- (2) Ferrari, M. Cancer Nanotechnology: Opportunities and Challenges. *Nat. Rev. Cancer* **2005**, *5*, 161–171.
- (3) Whitesides, G. M. Nanoscience, Nanotechnology, and Chemistry. *Small* **2005**, *1*, 172–179.
- (4) Weissleder, R. Scaling Down Imaging: Molecular Mapping of Cancer in Mice. *Nat. Rev. Cancer* **2002**, *2*, 11–18.

- (5) Margolis, D. J. A.; Hoffman, J. M.; Herfkens, R. J.; Jeffrey, R. B.; Quon, A.; Gambhir, S. S. Molecular Imaging Techniques in Body Imaging. *Radiology* **2007**, *245*, 333–356.
- (6) Sharma, P.; Brown, S.; Walter, G.; Santra, S.; Moudgil, B. Nanoparticles for Bioimaging. *Adv. Colloid Interface* **2006**, *123*, 471–485.
- (7) Park, Y. I.; Kim, H. M.; Kim, J. H.; Moon, K. C.; Yoo, B.; Lee, K. T.; Lee, N.; Choi, Y.; Park, W.; et al. Theranostic Probe Based on Lanthanide-Doped Nanoparticles for Simultaneous in Vivo Dual-Modal Imaging and Photodynamic Therapy. *Adv. Mater.* **2012**, *24*, 5755–5761.
- (8) Tassa, C.; Shaw, S. Y.; Weissleder, R. Dextran-Coated Iron Oxide Nanoparticles: A Versatile Platform for Targeted Molecular Imaging, Molecular Diagnostics, and Therapy. *Acc. Chem. Res.* **2011**, *44*, 842–852.
- (9) Gianella, A.; Jarzyna, P. A.; Mani, V.; Ramachandran, S.; Calcagno, C.; Tang, J.; Kann, B.; Dijk, W. J. R.; Thijssen, V. L.; et al. Multifunctional Nanoemulsion Platform for Imaging Guided Therapy Evaluated in Experimental Cancer. *ACS Nano* **2011**, *5*, 4422–4433.
- (10) Lee, N.; Hyeon, T. Designed Synthesis of Uniformly Sized Iron Oxide Nanoparticles for Efficient Magnetic Resonance Imaging Contrast Agents. *Chem. Soc. Rev.* **2012**, *41*, 2575–2589.
- (11) Banerjee, S. S.; Chen, D. H. A Multifunctional Magnetic Nanocarrier Bearing Fluorescent Dye for Targeted Drug Delivery by Enhanced Two-Photon Triggered Release. *Nanotechnology* **2009**, *20*, 18S103–18S111.
- (12) Wang, W.; Zou, M.; Chen, K. Z. Novel $\text{Fe}_3\text{O}_4/\text{YPO}_4:\text{Re}$ (Re = Tb, Eu) Multifunctional Magnetic-Fluorescent Hybrid Spheres for Biomedical Applications. *Chem. Commun.* **2010**, *46*, 5100–5102.
- (13) Li, I. F.; Yeh, C. S. Synthesis of Gd Doped CdSe Nanoparticles for Potential Optical and MR Imaging Applications. *J. Mater. Chem.* **2010**, *20*, 2079–2081.
- (14) Zeng, S. J.; Xiao, J. J.; Yang, Q. B.; Hao, J. H. Bi-Functional $\text{NaLuF}_4: \text{Gd}^{3+}/\text{Yb}^{3+}/\text{Tm}^{3+}$ Nanocrystals: Structure Controlled Synthesis, Near-Infrared Upconversion Emission and Tunable Magnetic Properties. *J. Mater. Chem.* **2012**, *22*, 9870–9874.
- (15) Schellenberger, E. A.; Sosnovik, D.; Weissleder, R.; Josephson, L. Magneto/Optical Annexin V, a Multimodal Protein. *Bioconjugate Chem.* **2004**, *15*, 1062–1067.
- (16) Ma, Z. Y.; Dosev, D.; Nichkova, M.; Gee, S. J.; Hammock, B. D.; Kennedy, I. M. Synthesis and Bio-Functionalization of Multifunctional Magnetic $\text{Fe}_3\text{O}_4/\text{Y}_2\text{O}_3:\text{Eu}$ Nanocomposites. *J. Mater. Chem.* **2009**, *19*, 4695–4700.
- (17) Mukherjee, P.; Shade, C. M.; Yingling, A. M.; Lamont, D. N.; Waldeck, D. H.; Petoud, S. A Post-Synthetic Modification of II-VI Nanoparticles to Create Tb^{3+} and Eu^{3+} Luminophores. *J. Phys. Chem. A* **2011**, *115*, 4031–4041.
- (18) Zeng, X. Y.; Yuan, J. L.; Zhang, L. D. Synthesis and Photoluminescent Properties of Rare Earth Doped ZnO Hierarchical Microspheres. *J. Phys. Chem. C* **2008**, *112*, 3503–3508.
- (19) Bouzigues, C.; Gacoin, T.; Alexandrou, A. Biological Applications of Rare-Earth Based Nanoparticles. *ACS Nano* **2011**, *5*, 8488–8505.
- (20) Auzel, F. Upconversion and Anti-Stokes Processes with f and d Ions in Solids. *Chem. Rev.* **2004**, *104*, 139–174.
- (21) Haase, M.; Schäfer, H. Nanopartikel für die Aufw rtskonversion. *Angew. Chem.* **2011**, *123*, 5928–5950.
- (22) Yu, X.; Li, M.; Xie, M.; Chen, L.; Li, Y.; Wang, Q. Dopant-Controlled Synthesis of Water-Soluble Hexagonal NaYF_4 Nanorods with Efficient Upconversion Fluorescence for Multicolor Bioimaging. *Nano Res.* **2010**, *3*, 51–60.
- (23) Chatterjee, D. K.; Gnanasammandhan, M. K.; Zhang, Y. Small Upconverting Fluorescent Nanoparticles for Biomedical Applications. *Small* **2010**, *6*, 2781–2795.
- (24) Cheng, L.; Yang, K.; Zhang, S.; Shao, M.; Lee, S. Highly-Sensitive Multiplexed in Vivo Imaging Using PEGylated Upconversion Nanoparticles. *Nano Res.* **2010**, *3*, 722–732.
- (25) Cheng, L.; Yang, K.; Li, Y. G.; Chen, J. H.; Wang, C.; Shao, M. W.; Lee, S. T.; Liu, Z. Facile Preparation of Multifunctional

Upconversion Nanoprobes for Multimodal Imaging and Dual-Targeted Photothermal Therapy. *Angew. Chem.* **2011**, *123*, 7523–7528.

(26) Liu, Y. L.; Ai, K. L.; Yuan, Q. H.; Lu, L. H. Fluorescence-Enhanced Gadolinium-Doped Zinc Oxide Quantum Dots for Magnetic Resonance and Fluorescence Imaging. *Biomaterials* **2011**, *32*, 1185–1192.

(27) Xu, Z. P.; Kurniawan, N. D.; Bartlett, P. F.; Lu, G. Q. Enhancement of Relaxivity Rates of Gd-DTPA Complexes by Intercalation into Layered Double Hydroxide Nanoparticles. *Chem.—Eur. J.* **2007**, *13*, 2824–2830.

(28) Wang, C.; Cheng, L.; Liu, Z. Drug Delivery with Upconversion Nanoparticles for Multi-Functional Targeted Cancer Cell Imaging and Therapy. *Biomaterials* **2011**, *32*, 1110–1120.

(29) Qian, H. S.; Guo, H. C.; Ho, P. C.-L.; Mahendran, R.; Zhang, Y. Mesoporous Silica Coated Upconversion Fluorescent Nanoparticles for Photodynamic Therapy. *Small* **2009**, *5*, 2285–2290.

(30) Chatterjee, D. K.; Fong, L. S.; Zhang, Y. Nanoparticles in Photodynamic Therapy: An Emerging Paradigm. *Adv. Drug Delivery Rev.* **2008**, *60*, 1627–1637.

(31) Bechet, D.; Couleaud, P.; Frochot, C.; Viriot, M. L.; Guillemain, F.; Barberi-Heyob, M. Exploring and Exploiting Carotenoid Accumulation in *Dunaliella Salina* for Cell-Factory Applications. *Trends Biotechnol.* **2008**, *26*, 631–638.

(32) Detty, M. R.; Gibson, S. L.; Wagner, S. J. Current Clinical and Preclinical Photosensitizers for Use in Photodynamic Therapy. *J. Med. Chem.* **2004**, *47*, 3897–3915.

(33) Lu, T.; Shao, P.; Mathew, I.; Sand, A.; Sun, W. F. Synthesis and Photophysics of Benzotetraphyrin: A Near-Infrared Emitter and Photosensitizer. *J. Am. Chem. Soc.* **2008**, *130*, 15782–15783.

(34) Ji, H. T.; Chien, L. T.; Lin, Y. H.; Chien, H. F.; Chen, C. T. Research 5-ALA Mediated Photodynamic Therapy Induces Autophagic Cell Death via AMP-Activated Protein Kinase. *Mol. Cancer* **2010**, *9*, 91–101.

(35) Cui, S. S.; Chen, H. Y.; Zhu, H. Y.; Tian, J. M.; Chi, X. M.; Qian, Z. Y.; Achileuf, S.; Gu, Y. Q. Amphiphilic Chitosan Modified Upconversion Nanoparticles for in Vivo Photodynamic Therapy Induced by Near-Infrared Light. *J. Mater. Chem.* **2012**, *22*, 4861–4873.

(36) Lee, S. J.; Koo, H.; Jeong, H.; Huh, M. S.; Choi, Y.; Jeong, S. Y.; Byun, Y.; Choi, K.; Kim, K.; Kwon, I. C. Comparative Study of Photosensitizer Loaded and Conjugated Glycol Chitosan Nanoparticles for Cancer Therapy. *J. Controlled Release* **2011**, *152*, 21–29.

(37) Shan, J.; Budijono, S. J.; Hu, G.; Yao, N.; Kang, Y.; Ju, Y.; Prud'homme, R. K. Pegylated Composite Nanoparticles Containing Upconverting Phosphors and Meso Tetraphenyl Porphine (TPP) for Photodynamic Therapy. *Adv. Funct. Mater.* **2011**, *21*, 2488–2495.

(38) Li, C.; Xu, Z.; Yang, D.; Cheng, Z.; Hou, Z.; Lin, J. Well-Dispersed KRE₃F₁₀ (RE = Sm-Lu, Y) Nanocrystals: Solvothermal Synthesis and Luminescence Properties. *CrystEngComm* **2011**, *14*, 670–678.

(39) Zhang, P.; Steelant, W.; Kumar, M.; Scholfield, M. Versatile Photosensitizers for Photodynamic Therapy at Infrared Excitation. *J. Am. Chem. Soc.* **2007**, *129*, 4526–4527.

(40) Wang, C.; Tao, H. Q.; Cheng, L.; Liu, Z. Near-Infrared Light Induced in Vivo Photodynamic Therapy of Cancer Based on Upconversion Nanoparticles. *Biomaterials* **2011**, *32*, 6145–6154.

(41) Chatterjee, D. K.; Zhang, Y. Upconverting Nanoparticles as Nanotransducers for Photodynamic Therapy in Cancer Cells. *Nanomedicine* **2008**, *3*, 73–82.

(42) Ungun, B.; Prud'homme, R. K.; Budijono, S. J.; Shan, J. N.; Lim, S. F.; Ju, Y. G.; Austin, R. Nanofabricated Upconversion Nanoparticles for Photodynamic Therapy. *Opt. Express* **2009**, *17*, 80–86.

(43) Park, Y. I.; Kim, H. M.; Kim, J. H.; Moon, K. C.; Yoo, B.; Lee, K. T.; Lee, N.; Choi, Y.; Park, W.; et al. Theranostic Probe Based on Lanthanide-Doped Nanoparticles for Simultaneous In Vivo Dual-Modal Imaging and Photodynamic Therapy. *Adv. Mater.* **2012**, *24*, S755–S761.

(44) Wang, C.; Cheng, L.; Liu, Y. M.; Wang, X. J.; Ma, X. X.; Deng, Z. Y.; Li, Y. G.; Liu, Z. Imaging-Guided pH-Sensitive Photodynamic

Therapy Using Charge Reversible Upconversion Nanoparticles Under Near-Infrared Light. *Adv. Funct. Mater.* **2013**, *23*, 3077–3086.

(45) Guo, H. C.; Qian, H. S.; Idris, N. M.; Zhang, Y. Singlet Oxygen-Induced Apoptosis of Cancer Cells Using Upconversion Fluorescent Nanoparticles as A Carrier of Photosensitizer. *Nanomedicine: NBM* **2010**, *6*, 486–495.

(46) Idris, N. M.; Gnanasammandhan, M. K.; Zhang, J.; Ho, P. C.; Mahendran, R.; Zhang, Y. In Vivo Photodynamic Therapy Using Upconversion Nanoparticles as Remote-Controlled Nanotransducers. *Nat. Med.* **2012**, *18*, 1580–1585.

(47) Corr, S. A.; Rakovich, Y. P.; Gun'ko, Y. K. Multifunctional Magnetic-Fluorescent Nanocomposites for Biomedical Applications. *Nanoscale Res. Lett.* **2008**, *3*, 87–104.

(48) Hong, H.; Shi, J.; Yang, Y. N.; Zhang, Y.; Engle, J. W.; Nickles, R. J.; Wang, X. D.; Cai, W. B. Cancer-Targeted Optical Imaging with Fluorescent Zinc Oxide Nanowires. *Nano Lett.* **2011**, *11*, 3744–3750.

(49) Wang, Z. L. Splendid One-Dimensional Nanostructures of Zinc Oxide: A New Nanomaterial Family for Nanotechnology. *ACS Nano* **2008**, *2*, 1987–1992.

(50) Geng, J.; Liu, B.; Xu, L.; Hu, F. N.; Zhu, J. J. Facile Route to Zn-Based II-VI Semiconductor Spheres, Hollow Spheres, and Core/Shell Nanocrystals and Their Optical Properties. *Langmuir* **2007**, *23*, 10286–10293.

(51) Wang, X. D.; Summers, C. J.; Wang, Z. L. Large-Scale Hexagonal-Patterned Growth of Aligned ZnO Nanorods for Nano-Optoelectronics and Nanosensor Arrays. *Nano Lett.* **2004**, *4*, 423–426.

(52) Park, W. I.; Yi, G. C. Electroluminescence in n-ZnO Nanorod Arrays Vertically Grown on p-GaN. *Adv. Mater.* **2004**, *16*, 87–90.

(53) Sharma, P.; Brown, S.; Walter, G.; Santra, S.; Moudgil, B. Nanoparticles for Bioimaging. *Adv. Colloid Interface* **2006**, *123*, 471–485.

(54) Zhang, P.; Liu, W. ZnO QD@PMAA-co-PDMAEMA Nonviral Vector for Plasmid DNA Delivery and Bioimaging. *Biomaterials* **2010**, *31*, 3087–3094.

(55) Barcena, C.; Sra, A. K.; Chaubey, G. S.; Khemtong, C.; Liu, J. P.; Gao, J. Biomimetic Subwavelength Antireflective Gratings on GaAs. *Chem. Commun.* **2008**, *19*, 2224–2226.

(56) Chang, C. C.; Chiu, N. F.; Lin, D. S.; Chu-Su, Y.; Liang, Y. H.; Lin, C. W. High-Sensitivity Detection of Carbohydrate Antigen 15–3 Using a Gold/Zinc Oxide Thin Film Surface Plasmon Resonance-Based Biosensor. *Anal. Chem.* **2010**, *82*, 1207–1212.

(57) Barick, K. C.; Aslam, M.; Dravid, V. P.; Bahadur, D. Self-Aggregation and Assembly of Size-Tunable Transition Metal Doped ZnO Nanocrystals. *J. Phys. Chem. C* **2008**, *112*, 15163–15170.

(58) Barick, K. C.; Nigam, S.; Bahadur, D. Nanoscale Assembly of Mesoporous ZnO: A Potential Drug Carrier. *J. Mater. Chem.* **2010**, *20*, 6446–6452.

(59) Sommerdijk, J. L. On The Excitation Mechanisms of The Infrared-Excited Visible Luminescence in Yb³⁺, Er³⁺-doped Fluorides. *J. Lumin.* **1971**, *4*, 441–449.

(60) Wang, X.; Kong, X.; Yu, Y.; Sun, Y. J.; Zhang, H. Effect of Annealing on Upconversion Luminescence of ZnO:Er³⁺ Nanocrystals and High Thermal Sensitivity. *J. Phys. Chem. C* **2007**, *111*, 15119–15124.

(61) Zhang, F.; Zhao, D. Fabrication of Ordered Magnetite-doped Rare Earth Fluoride Nanotube Arrays by Nanocrystal Self-assembly. *Nano Res.* **2009**, *2*, 292–305.

(62) Luo, W. Q.; Fu, C. Y.; Li, R. F.; Liu, Y. S.; Zhu, H. M.; Chen, X. Y. Er³⁺ Doped Anatase TiO₂ Nanocrystals: Crystal-Field Levels, Excited-State Dynamics, Upconversion, and Defect Luminescence. *Small* **2011**, *7*, 3046–3056.

(63) Zeng, H.; Duan, G.; Cai, W. P.; Li, Y.; Yang, S. K.; Xu, X. X. Blue Luminescence of ZnO Nanoparticles Based on Non-Equilibrium Processes: Defect Origins and Emission Controls. *Adv. Funct. Mater.* **2010**, *20*, S61–S72.

(64) Zhang, X. Y.; Lu, L. P.; Bo, C. H.; Liu, Q. S.; Yang, K. S. Rare Earth Luminescent Materials. *National Defence Industry Press* **2005**, P14.

- (65) Wang, X.; Kong, X.; Yu, Y.; Zhang, H. Synthesis and Characterization of Water-Soluble and Bifunctional ZnO-Au Nanocomposites. *J. Phys. Chem. C* **2007**, *111*, 3836–3841.
- (66) Ren, G. Z.; Zeng, S. J.; Hao, J. H. Tunable Multicolor Upconversion Emissions and Paramagnetic Property of Monodispersed Bifunctional Lanthanide-Doped NaGdF₄ Nanorods. *J. Phys. Chem. C* **2011**, *115*, 20141–20147.
- (67) Wang, L. Y.; Li, Y. D. Controlled Synthesis and Luminescence of Lanthanide Doped NaYF₄ Nanocrystals. *Chem. Mater.* **2007**, *19*, 727–734.
- (68) Matsuura, D. Red, Green, and Blue Upconversion Luminescence of Trivalent Rare Earth Ion Doped Y₂O₃ Nanocrystals. *Appl. Phys. Lett.* **2002**, *81*, 4526–4528.
- (69) Yang, P. H.; Sun, X. S.; Chiu, J. F.; Sun, H. Z.; He, Q. Y. Transferrin-Mediated Gold Nanoparticle Cellular Uptake. *Bioconjugate Chem.* **2005**, *16*, 494–496.
- (70) Li, H.; Sun, H.; Qian, Z. M. The Role of The Transferrin-Transferrin-Receptor System in Drug Delivery and Targeting. *Trends Pharmacol. Sci.* **2002**, *23*, 206–209.
- (71) Rao, G. C.; Kumar, M. S.; Mathivanan, N.; Rao, M. E. Nanosuspensions as The Most Promising Approach in Nanoparticulate Drug Delivery Systems. *Pharmazie* **2004**, *59*, 5–9.
- (72) Portlock, J. L.; Calos, M. P. Site-Specific Genomic Strategies for Gene Therapy. *Curr. Opin. Mol. Ther.* **2003**, *5*, 376–382.
- (73) Russell-Jones, G. J. The Potential Use of Receptor Mediated Endocytosis for Oral Drug Delivery. *Adv. Drug Delivery Rev.* **2001**, *46*, 59–73.
- (74) Qian, Z. M.; Li, H.; Sun, H.; Ho, K. Targeted Drug Delivery via The Transferrin Receptor-Mediated Endocytosis Pathway. *Pharmacol. Rev.* **2002**, *54*, 561–587.
- (75) Jordan, F. L.; Wynder, H. J.; Booth, P. L.; Thomas, W. E. Method for The Identification of Brain Macrophages/Phagocytic Cells in Vitro. *J. Neurosci. Res.* **1990**, *26*, 74–82.
- (76) Stringer, B.; Imrich, A.; Kobzik, L. Flow Cytometric Assay of Lung Macrophage Uptake of Environmental Particulates. *Cytometry* **1995**, *20*, 23–32.
- (77) Wei, W.; Wang, L. Y.; Yuan, L.; Wei, Q.; Yang, X. D.; Su, Z. G.; Ma, G. H. Preparation and Application of Novel Microspheres Possessing Autofluorescent Properties. *Adv. Funct. Mater.* **2007**, *17*, 3153–3158.
- (78) Hackbarth, S.; Schlothauer, J.; Preuss, A.; Roder, B. New Insights to Primary Photodynamic Effects-Singlet Oxygen Kinetics in Living Cells. *J. Photochem. Photobiol. B* **2010**, *98*, 173–179.
- (79) Juarranz, A.; Jaen, P.; Sanz-Rodriguez, F.; Cuevas, J.; Gonzalez, S. Photodynamic Therapy of Cancer: Basic Principles and Applications. *Clin. Transl. Oncol.* **2008**, *10*, 148–154.
- (80) Starkey, J. R.; Rebane, A. K.; Drobizhev, M. A.; Meng, F.; Gong, A.; Elliott, A.; McInnerney, K.; Spangler, C. W. New Two-Photon Activated Photodynamic Therapy Sensitizers Induce Xenograft Tumor Regressions After Near-IR Laser Treatment Through The Body of The Host Mouse. *Clin. Cancer Res.* **2008**, *14*, 6564–6573.
- (81) Wang, F.; Banerjee, D.; Liu, Y. S.; Chen, X. Y.; Liu, X. G. Upconversion Nanoparticles in Biological Labeling, Imaging, and Therapy. *Analyst* **2010**, *135*, 1839–1854.
- (82) Tuite, E. M.; Kelly, J. M. New Trends in Photobiology: Photochemical Interactions of Methylene Blue and Analogues with DNA and other Biological Substrates. *J. Photochem. Photobiol. B* **1993**, *21*, 103–124.
- (83) Kaplan, J. C.; Chirouze, M. Therapy of Recessive Congenital Methaemoglobinemia by Oral Riboflavine. *Lancet* **1978**, *312*, 1043–1044.
- (84) Wright, R. O.; Lewander, W. J.; Woolf, A. D. Methemoglobinemia: Etiology, Pharmacology, and Clinical Management. *Ann. Emerg. Med.* **1999**, *34*, 646–656.
- (85) Redmond, R. W.; Gamlin, J. N. A Compilation of Singlet Oxygen Yields From Biologically Relevant Molecules. *Photochem. Photobiol.* **1999**, *70*, 391–475.
- (86) Chen, F.; Zhang, S. J.; Bu, W. B.; Chen, Y.; Xiao, Q. F.; Liu, J. N.; Xing, H. Y.; Zhou, L. P.; Peng, W. J.; et al. A Uniform Sub 50 nm Sized Magnetic/Upconversion Fluorescent Bimodal Imaging Agent Capable of Generating Singlet Oxygen by Using a 980 nm Laser. *Chem.—Eur. J.* **2012**, *18*, 7082–7090.
- (87) Sasaki, M.; Shi, E.; Kanbara, Y.; Ehara, S.; Reson, M. Enhancement Effects and Relaxivities of Gadolinium-DTPA at 1.5 Versus 3 T: A Phantom Study. *Med. Sci.* **2005**, *4*, 145–149.
- (88) Roch, A.; Muller, R. N.; Gillis, P. Theory of Proton Relaxation Induced by Superparamagnetic Particles. *J. Chem. Phys.* **1999**, *110*, 5403–5411.
- (89) Aime, S.; Botta, M.; Fasano, M.; Terreno, E. Lanthanide(III) Chelates for NMR Biomedical Applications. *Chem. Soc. Rev.* **1998**, *27*, 19–29.
- (90) Yang, C. T.; Chuang, K. H. Gd(III) Chelates for MRI Contrast Agents: From High Relaxivity to “Smart”, From Blood Pool to Blood-Brain Barrier Permeable. *Med. Chem. Commun.* **2012**, *3*, 552–565.
- (91) Werner, E. J.; Datta, A.; Jocher, C. J.; Raymond, K. N. High-Relaxivity MRI Contrast Agents: Where Coordination Chemistry Meets Medical Imaging. *Angew. Chem., Int. Ed.* **2008**, *47*, 8568–8580.
- (92) Chen, F.; Bu, W.; Zhang, S.; Liu, J.; Fan, W.; Zhou, L.; Peng, W. J.; Shi, J. Gd³⁺-Ion-Doped Upconversion Nanoprobes: Relaxivity Mechanism Probing and Sensitivity Optimization. *Adv. Funct. Mater.* **2013**, *23*, 298–307.
- (93) Kim, T.; Momin, E.; Choi, J.; Yuan, K.; Zaidi, H.; Kim, J.; Gilad, A. A.; et al. Mesoporous Silica-Coated Hollow Manganese Oxide Nanoparticles as Positive T₁ Contrast Agents for Labeling and MRI Tracking of Adipose-Derived Mesenchymal Stem Cells. *J. Am. Chem. Soc.* **2011**, *133*, 2955–2961.
- (94) Cheng, Z. L.; Thorek, D. L. J.; Tsourkas, A. Porous Polymersomes with Encapsulated Gd-Labeled Dendrimers as Highly Efficient MRI Contrast Agents. *Adv. Funct. Mater.* **2009**, *19*, 3753–3759.